Environmental Science and Ecotechnology 21 (2024) 100416

Contents lists available at ScienceDirect

Environmental Science and Ecotechnology

journal homepage: www.journals.elsevier.com/environmental-science-and-ecotechnology/

Original Research

Cobalt single-atom catalyst tailored ceramic membrane for selective removal of emerging organic contaminants

Jiaxuan Yang [a], Jing Zhao [a], Hesong Wang [a], Yatao Liu [b], Junwen Ding [a], Tianyi Wang [a], Jinlong Wang [a], Han Zhang [a], Langming Bai [a], Heng Liang [a, *]

[a] State Key Laboratory of Urban Water Resource and Environment, School of Environment, Harbin Institute of Technology, Harbin, 150090, PR China
[b] Beijing Key Laboratory for Source Control Technology of Water Pollution, College of Environmental Science and Engineering, Beijing Forestry University, Beijing, 100083, PR China

ARTICLE INFO

Article history:
Received 30 September 2023
Received in revised form
15 March 2024
Accepted 16 March 2024

Keywords:
Single-atom catalytic ceramic membrane
Peroxymonosulfate activation
Selective oxidation
Interfacial response
Multi-layer functional zones

ABSTRACT

Water reuse is an effective way to solve the issues of current wastewater increments and water resource scarcity. Ultrafiltration, a promising method for water reuse, has the characteristics of low energy consumption, easy operation, and high adaptability to coupling with other water treatment processes. However, emerging organic contaminants (EOCs) in municipal wastewater cannot be effectively intercepted by ultrafiltration, which poses significant challenges to the effluent quality and sustainability of ultrafiltration process. Here, we develop a cobalt single-atom catalyst-tailored ceramic membrane (Co_1-NCNT-CM) in conjunction with an activated peroxymonosulfate (PMS) system, achieving excellent EOCs degradation and anti-fouling performance. An interfacial reaction mechanism effectively mitigates membrane fouling through a repulsive interaction with natural organic matter. The generation of singlet oxygen at the Co-N_3-C active sites through a catalytic pathway (PMS → PMS* → OH* → O* → OO* → $^1O_2$) exhibits selective oxidation of phenols and sulfonamides, achieving >90% removal rates. Our findings elucidate a multi-layered functional architecture within the Co_1-NCNT-CM/PMS system, responsible for its superior performance in organic decontamination and membrane maintenance during secondary effluent treatment. It highlights the power of integrating Co_1-NCNT-CM/PMS systems in advanced wastewater treatment frameworks, specifically for targeted EOCs removal, heralding a new direction for sustainable water management.

1. Introduction

Water recycling strategies are effective ways to solve the scarcity of freshwater resources, in which wastewater reuse may promote the development of wastewater as an alternative water source [1]. However, various emerging organic contaminants (EOCs), such as phenols, antibiotics, pharmaceuticals, pesticides, and personal care products, have recently been frequently monitored in municipal wastewater, posing new challenges to wastewater reuse technologies [2,3]. Hence, research on promising and novel technologies is urgent to satisfy the current wastewater reuse needs and sustainable development goals. Although ultrafiltration (UF) membrane processes with land saving, chemical use reduction and modular configuration have become essential components for wastewater reuse [4], the problems of membrane fouling and inferior rejection of EOCs have gradually limited their application [5,6]. As a disruptive innovation in the twenty-first century, nanotechnology may provide a leap-forward opportunity to develop membrane technologies in wastewater reuse, which is expected to break through the bottlenecks of current UF processes [7,8].

Compatibility of nanotechnologies with UF processes requires consideration of the functional orientation of nanomaterials during the coupling process. In this regard, metal nanomaterials with catalytic properties offer opportunities to UF technologies in EOCs degradation and self-cleaning [9,10]. The peroxymonosulfate (PMS) activation processes with metal nanocatalysts (especially Co-based catalysts) as the core recently attracted widespread attention due to their advantages, such as high reactivity, simple separation, and low cost [11]. Nevertheless, the coordination structure of Co atoms is inferiorly tunable in traditional heterogeneous Co-based

* Corresponding author.
E-mail address: hitliangheng@163.com (H. Liang).

https://doi.org/10.1016/j.ese.2024.100416

catalysts, affecting the catalytic performance [12]. In contrast, Co single-atom catalysts (SACs), the heterogeneous catalysts with atomically dispersed metal active sites, can compensate for shortcomings [13]. It is reported that Co-SACs/PMS exhibited a strong catalytic capacity, which is 2–4 orders of magnitude greater than that of Co^{2+}/PMS and Co_3O_4/PMS systems [12]. Furthermore, appropriate carriers can restrict the agglomeration of Co atoms by stable anchoring centers to further promote the efficiency of Co-based SACs [14]. Among them, N-doped carbon matrixes, including graphene, metal-organic frameworks, and carbon nanotubes (CNT), are generally more stable to anchor Co atoms as electron-rich N-doped sites generate the Lewis-base that tends to interact with metal sites [15]. The positively charged carbon domains caused by N doping are also conducive to stimulating the formation of non-radical pathways with higher tolerance to water matrices [16]. Wang et al. engineered the Co-N_3O_1 sites on tubular carbon nitride to modulate the selective singlet oxygen ($^1O_2$) production, achieving 97.5% removal of ciprofloxacin [17]. However, the undesired agglomeration of the carbon matrixes themselves results in limited available active sites, reducing PMS-organics-catalysts' mass transfer efficiency [18].

To solve the problems above, loading SACs on the membrane to form the catalytic membrane is an effective strategy, which concentrates reactive substances and shortens transfer paths to enhance the mass transfer of surface-dominated reactions [19]. Meanwhile, single atom catalytic layer of the membrane activates PMS to generate abundant reactive species, achieving degradation of EOCs and natural organic matter (NOM) and membrane fouling mitigation. Besides, in terms of membrane materials, ceramic membranes (CM) with outstanding anti-oxidation properties are the optimal choice for integrating with the Co-SACs/PMS catalytic system [10]. Currently, reported modified CM is generally functionalized with metal nanocrystals or oxides, such as Co_3O_4 [20], $CuFe_2O_4$ [21], and Co_3O_4-CNT [18], which limit metal atomic utilization. In addition, a few studies on single-atom catalytic membranes have been reported, all of which focus on the degradation of single micropollutants, such as designing Co_1-graphene oxide- and Cu_1-modified organic membranes to remove 1,4-dioxane and paracetamol [22,23]. Although many researchers have proposed the idea of technically coupling Co-SACs and CM in research prospects, the relevant coupling processes have rarely been reported. Besides, few studies have focused on the compatibility and adaptability of Co-SACs and CM technologies in the actual water environment. The interfacial response mechanism between contaminants and SACs-tailored CM during catalytic filtration has also not been investigated.

In this work, we designed a novel N-doped CNT-supported Co single-atom modified CM (Co_1-NCNT-CM) for PMS activation to remove some representative EOCs and treat secondary effluent. The Co-N coordination environment and Co species in the Co_1-NCNT catalyst and the effect of catalyst introduction on the CM were first determined. In addition, the compatibility and adaptability of Co_1-NCNT-CM in the actual water environment were assessed by studying the phenols and sulfonamides selective removal, NOM degradation, and membrane filtration performance in secondary effluent. The contributions of the Co_1-NCNT-CM repulsive functional zone were identified via the Extended Derjaguin-Landau-Verwey-Overbeek (XDLVO) theory. The working mechanisms of the oxidative functional zone were elucidated by revealing selective degradation principles and evolutionary pathways of key reactive species. Co_1-NCNT-CM/PMS may serve as a reserve technology for wastewater remediation and promote demand-oriented water treatment technology revolutions.

2. Materials and methods

2.1. Chemicals and reagents

Multi-walled carbon nanotubes (CNT) with 30–50 nm diameter and 10 μm length were purchased from Jiangsu XFNANO Materials Technology Co., Ltd (China). This study utilized the 50 kDa flat-sheet CM (TAMI, France) as the substrate. The structure of the CM included the support layer and active separation layer. Among them, the material of the support layer was TiO_2, and the material of the active separation layer was TiO_2/ZrO_2. The details of other chemicals and reagents were provided in Text S1. We prepared 10 mg L^{-1} of phenol, 2,4-dichlorophenol (2,4-DCP), bisphenol A (BPA), bisphenol F (BPF), paracetamol (APAP), sulfamethoxazole (SMX), sulfamethazine (SMZ), sulfadiazine (SDZ), sulfathiazole (STZ) solutions and 5 mg L^{-1} of atrazine (ATZ) and carbamazepine (CBZ) solutions in phosphate-buffered solution with a pH 7 for the catalytic filtration experiments. The secondary effluent (SE) was employed as actual water, which was obtained from the Wenchang wastewater treatment plant (Heilongjiang, China). The dissolved organic carbon and pH of the SE were 6.75 ± 0.21 mg L^{-1} and 7.42 ± 0.25, respectively.

2.2. Preparation and characterization of Co_1-NCNT and Co_1-NCNT-CM

First, 1 g CNT was dispersed in 200 mL of nitric acid (30 wt%) and heated to 100 °C for 2 h to remove residual metals in CNT. The obtained CNT was washed several times with Milli-Q water until neutral and dried in an oven at 60 °C. Afterward, 100 mg washed CNT was dispersed in 100 mL methanol (MeOH) mixed solution (30 mL Milli-Q water and 70 mL methanol) and sonicated for 10 min (suspension A). 21.11 mg cobalt acetate tetrahydrate and 17.80 mg citric acid monohydrate were dissolved in 10 mL Milli-Q water and sonicated for 10 min (solution B). Subsequently, 300 mg melamine and 1 mL solution B were added to suspension A, sonicated for 30 min, stirred and dried in a water bath at 100 °C, and ground to obtain a homogeneous mixture. Then, the mixture was placed in a tube furnace under an argon atmosphere at a heating rate of 5 °C min^{-1} to 700 °C for 1 h to obtain Co_1-NCNT catalyst. Other preparation procedures remained unchanged; NCNT was obtained without adding solution B, and CoCNT was obtained without adding melamine. Co_1-NCNT-CM was synthesized via coating Co_1-NCNT on the CM surface. Specifically, CM was washed with phosphoric acid, sodium hydroxide, and Milli-Q water and dried in an oven at 105 °C for 24 h. A certain amount of Co_1-NCNT was dispersed in 60 mL Milli-Q water and ultrasonicated through the ultrasonic cell grinder for 15 min. Then, this suspension was dead-end filtered onto the CM surface under a constant pressure of 0.1 MPa, and the resultant deposited membrane was dried in a vacuum oven at 60 °C. The preparation procedures of CNT-CM, NCNT-CM, and CoCNT-CM were similar.

Moreover, Raman spectroscopy (Raman), X-ray diffraction (XRD), X-ray photoelectron spectroscopy (XPS), scanning electron microscopy (SEM), atomic force microscopy (AFM), X-ray absorption near-edge structure (XANES) and extended X-ray fine structure (EXAFS) measurements, and inductively coupled plasma optical emission spectrometer (ICP-OES) were performed to characterize them, and details in Text S2.

2.3. Experimental procedure

A schematic diagram of the Co_1-NCNT-CM/PMS catalytic filtration is displayed in Fig. S1. The Co_1-NCNT-CM was placed at the end of the UF cell, and the untreated solution was poured into that.

Nitrogen provided a constant pressure of 0.06 MPa to drive the solution through the Co_1-NCNT-CM in the dead-end filtration mode. The weight of the treated solution was recorded every 6 s through electronic balance combined with a computer system. As for hydraulic backwashing, the utilized membrane was inverted into the UF cell after the filtration, and then 20 mL Milli-Q water was filtered. Sodium thiosulfate solution was added to the permeate to stop the oxidation reaction when the samples were collected.

2.4. Analytical methods

The concentrations of phenol, 2,4-DCP, BPA, BPF, APAP, SMX, SMZ, SDZ, STZ, CBZ, and ATZ were detected by the high-performance liquid chromatography (HPLC, Agilent 1200 LC, USA). The specific detection methods are summarized in Table S1. Besides, SE organic matter was monitored by excitation-emission matrix (EEM), and maximum fluorescence intensity (F_{max}) was quantified via parallel factor analysis [10]. Quenching experiments and electron paramagnetic resonance (EPR) were applied to identify the reactive species. Detailed information is shown in Text S3.

Moreover, the Resistance-in-series Model was employed to analyze membrane fouling resistances [24]. Structural optimizations of catalysts and relevant calculations of the Co_1-NCNT-CM/PMS system were carried out through the Vienna ab initio simulation package (VASP) based on density functional theory (DFT) [25]; Text S4 for details. The interfacial responses between NOM and membrane were analyzed according to XDLVO theory [26,27]. The van der Waals interaction energy (U^{LW}), electrostatic interaction energy (U^{EL}), and acid-base interaction energy (U^{AB}) with various separation distances were quantified [28,29]. Calculation formulas were illustrated in Text S5. The fitting analysis of the pore blocking-cake layer filtration combined model was conducted to clarify the membrane fouling filtration mechanism [30]. The obtained fitted data were utilized to plot d^2t/dV^2 and dt/dV curves based on the Hermia model [31], gaining the fouling mechanism index n value. The n values were 0, 1.0, 1.5, and 2.0, corresponding to the cake filtration, intermediate blocking, standard blocking, and complete blocking models (Text S6).

3. Results and discussion

3.1. Characterization of Co_1-NCNT and Co_1-NCNT-CM

The XRD patterns of CNT, NCNT, and Co_1-NCNT revealed two characteristic diffraction peaks at 25.9° and 43.0°, indexing to the (002) and (111) planes of the hexagonal graphitic carbon structure (Fig. S2) [32]. The XRD peaks of the three catalytic materials were located at similar positions, suggesting that the doping of cobalt and nitrogen did not destroy the original crystal structure of CNT. In addition, no Co foil peaks were observed for Co_1-NCNT nanomaterials, indicating that Co may be chemically coordinated on the CNT matrix in single atoms. Raman spectra of CNT and Co_1-NCNT (Fig. 1a) displayed the D-band at 1341 cm^{-1} and the G-band at 1571 cm^{-1}, referring to defective/disordered and graphitic carbon [33]. The higher intensity ratios of D-band and G-band ($I_D/I_G = 0.96$) for Co_1-NCNT confirmed that the as-prepared catalyst had more abundant defect structures than CNT ($I_D/I_G = 0.81$). XPS spectra of Co_1-NCNT (Fig. S3a) observed the characteristic peaks of C 1s, N 1s, and Co 2p, showing the successful doping of N and Co elements. In the C 1s spectrum (Fig. S3b), the peak at 285.6 eV (C-N) demonstrated the coordination between N and C [34]. N 1s spectrum of Co_1-NCNT (Fig. 1b) exhibited five deconvoluted peaks at 398.3, 399.0, 400.0, 401.4, and 405.4 eV, ascribing to pyridinic-N, the Co-N_x coordination, pyrrolic-N, graphitic-N, and oxide-N, respectively [35]. As depicted in Fig. S4, the introduction of Co resulted in a significant decrease in the proportion of pyridinic-N from 47.67% to 12.92%, suggesting that pyridinic-N may coordinate with Co dopants. The Co $2p_{3/2}$ spectrum of Co_1-NCNT showed two characteristic peaks at 781.5 and 786.8 eV (Fig. 1c), corresponding to Co-N_x coordination and satellite peak [36]. It could be speculated that the Co-N_x-C structure existed in the Co_1-NCNT.

XANES and EXAFS measurements were conducted to evaluate the chemical state and coordination environment of Co atoms in the Co_1-NCNT catalyst further. As illustrated in Fig. 1d, the Co K-edge XANES spectrum manifested that the absorption edge position of Co_1-NCNT was located between Co foil and CoO, which was closer to CoO. This indicated the valence state of the Co atoms in the Co_1-NCNT catalyst was positively charged and probably +2. A linear relationship between the main absorption edge and the oxidation states (Fig. S5a) also supported that Co had a near +2 valence state [37]. The Fourier-transform (FT) k^3-weighted EXAFS spectrum of Co_1-NCNT in Fig. 1e presented a dominant peak at 1.44 Å, which could be labeled as the Co-N first coordination shell. Notably, the Co-N coordination value in the Co_1-NCNT catalyst was relatively low, and the crystalline was inferior since its peak intensity was lower than that of CoPc [38,39]. Furthermore, no peaks of Co-Co and Co-O coordination were observed at 2.18 Å and 1.5 Å in Co_1-NCNT, demonstrating that Co nanoparticles and oxides were not generated. The EXAFS fitting results (Fig. 1f and S5b) of the Co-N first shell in Co_1-NCNT gave an average coordination number of 3.1 and an average bond length of 1.94 Å for the Co-N bond (Table S2). Compared to high coordination, low coordination catalysts may possess relatively high catalyst performance caused by the unique localized electronic structures and low free energy barriers [40]. Wavelet-transform (WT) spectrum in Fig. 1g investigated the atomic dispersion of Co species in Co_1-NCNT. The maximum intensity of Co_1-NCNT catalyst at ~4.0 $Å^{-1}$ was significantly close to Co-N peak in CoPc, which was clearly distinguished from Co foil (~7.1 $Å^{-1}$) and CoO (~6.1 $Å^{-1}$). This further confirmed the absence of Co nanoparticles and oxides in the catalytic material. The above results corroborated that the N-doped CNT anchored by single Co atoms was successfully prepared. The lower-coordinated Co-N_3-C structure formed by the coordination of a single Co atom with three pyridinic-N atoms existed in the Co_1-NCNT catalyst.

SEM and AFM were applied to characterize the microstructure of pristine CM and Co_1-NCNT-CM. As shown in Fig. 1h, the surface of the Co_1-NCNT-CM was completely covered by the catalytic nanomaterials, which was different from that of the pristine CM. EDS spectrum of Co_1-NCNT-CM (Fig. 2a) stated that N and Co elements were uniformly distributed on the membrane surface. The cross-section structure of the Co_1-NCNT-CM was illustrated in Fig. 2b, and the coating thickness of nano-catalysts was approximately 10 μm. Three-dimensional AFM images (Fig. 2c and d) depicted that the average roughness of the Co_1-NCNT-CM surface increased from 24.4 nm of pristine CM to 41.2 nm (Table S3). Additionally, as shown from Fig. S6, the pure water permeate flux between pristine CM and Co_1-NCNT-CM was almost the same. These cases may be due to that the size of the nanomaterials deposited on the CM surface was much larger than the CM pore size [41,42]. Hence, the deposited layer of nano-catalysts had a certain effect on the roughness of membrane surfaces rather than the water permeate flux.

3.2. Effects of Co_1-NCNT-CM/PMS on EOCs

The doping amount of single Co atoms (0.5 wt%), the loading amount of the catalyst (0.2 mg cm^{-2}), and the dosage of PMS (0.3 mM) were optimized and determined (Text S7 and Fig. S7), which were important factors affecting the catalytic filtration performance. Moreover, eleven representative EOCs were selected to

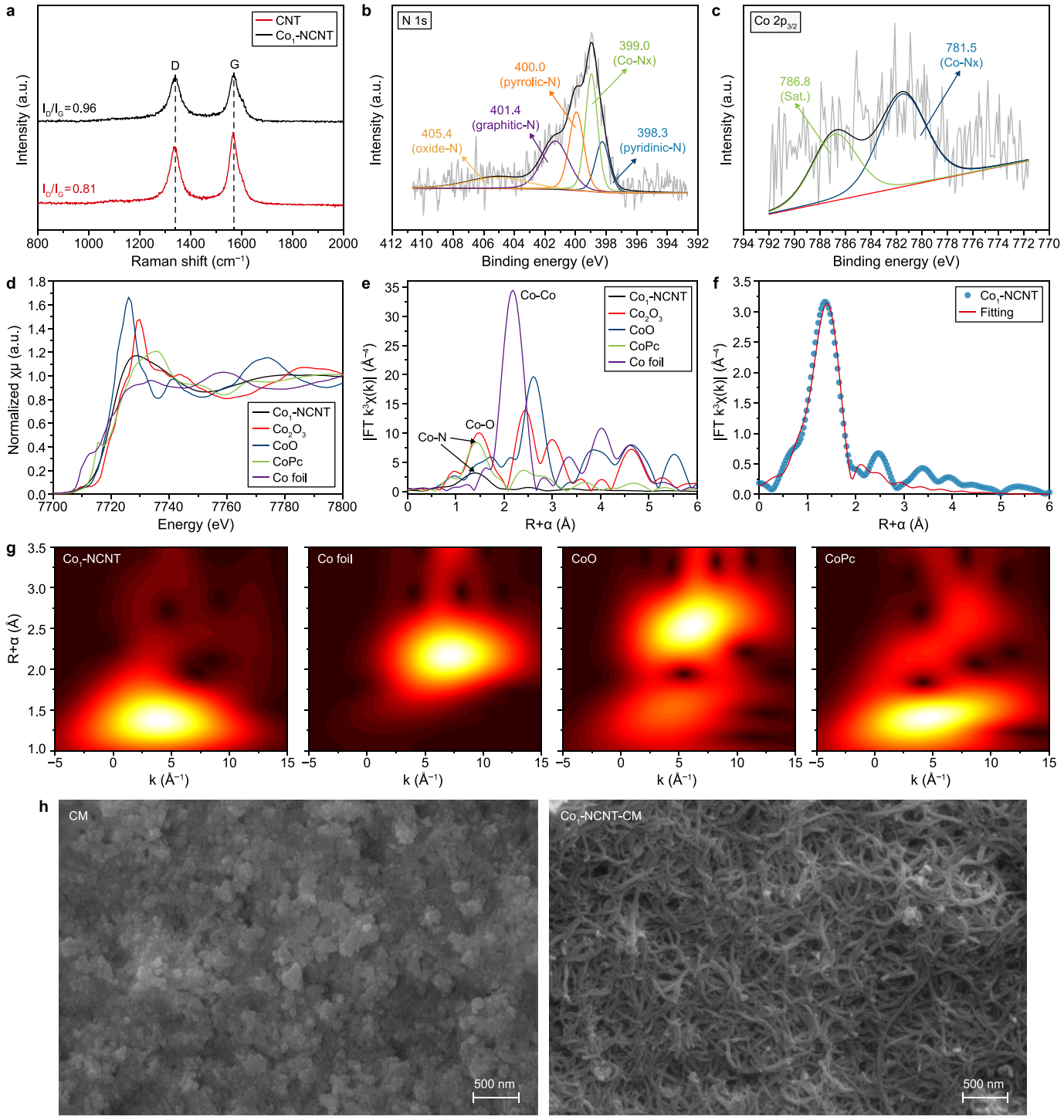

Fig. 1. **a**, Raman spectra of CNT and Co_1-NCNT. **b**–**c**, XPS spectra of Co_1-NCNT: N 1s (**b**) and Co 2p (**c**). **d**, Normalized Co K-edge XANES spectra of Co_1-NCNT and reference samples. **e**, Co K-edge FT-EXAFS spectra of Co_1-NCNT and reference samples in R-space. **f**, Corresponding FT-EXAFS fitting curves of Co_1-NCNT in R space. **g**, WT contour map of Co_1-NCNT and reference samples. **h**, SEM images of CM and Co_1-NCNT-CM surface.

examine the stability and oxidation properties of the Co_1-NCNT-CM/PMS system.

As illustrated in Fig. 3a, the CM/PMS process was negligible for removing phenol due to its small molecule refractory characteristics that cannot be trapped by CM and oxidized by PMS [24]. CNT-CM/PMS slightly improved phenol degradation and increased the removal rate to 15.50% at 15 min. CM modified by CNT doped with N atom and Co nanoparticles exhibited a better phenol removal (25.59–37.85%) at 15 min. This was consistent with previous reports that introducing some heteroatoms enhanced the PMS activation efficiency [43]. Particularly, Co_1-NCNT-CM/PMS showed the greatest degradation on phenol, reaching approximately 100% removal with no change within 15 min. Remarkably, the concentration of phenol gradually increased with the reaction time on

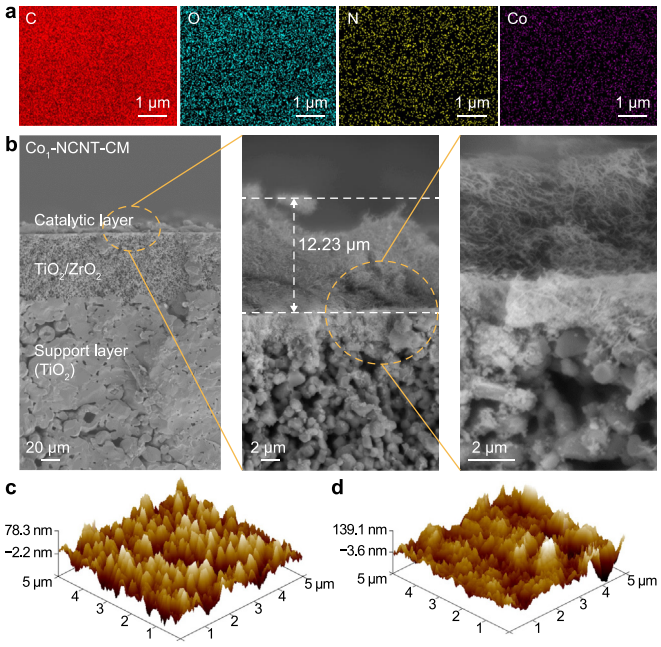

Fig. 2. **a**, EDS mapping images of Co_1-NCNT-CM surface. **b**, SEM images of Co_1-NCNT-CM cross-section. **c**–**d**, AFM images of CM (**c**) and Co_1-NCNT-CM (**d**).

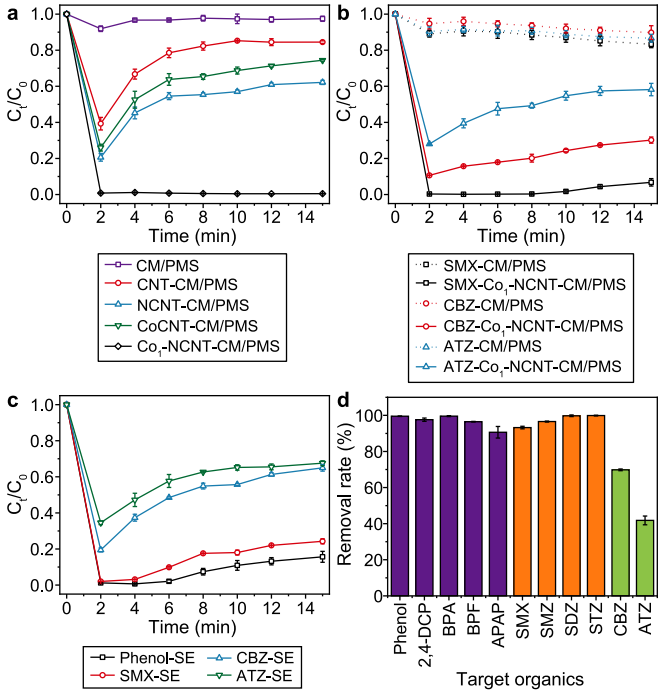

Fig. 3. **a**, Removal of phenol by different treatment groups. **b**, Removal of SMX, CBZ, and ATZ by Co_1-NCNT-CM/PMS. **c**, Removal of contaminants in the SE matrix. **d**, Removal rate of other phenolic (phenol, 2,4-DCP, BPA, BPF, APAP) and sulfonamide organics (SMX, SMZ, SDZ, STZ) at 15 min. Reaction conditions: [phenol] = [2,4-DCP] = [BPA] = [BPF] = [APAP] = [SMX] = [SMZ] = [SDZ] = [STZ] = 10 mg L^{-1}, [CBZ] = [ATZ] = 5 mg L^{-1}, [PMS] = 0.3 mmol L^{-1}, pH = 7, temperature = 20 °C. Error bars were standard deviations (n = 3).

some occasions because (1) the adsorption saturation of the modified CM and (2) the active sites of the catalyst were fouled by refractory organics. This work found that the catalytic systems generally achieved relatively stable degradation after 10 min. A similar situation occurred when Cheng et al. and Liu et al. deposited Co_3O_4 and NCNT onto membranes for methylene blue and phenol removal [18,41]. Furthermore, the stability of Co_1-NCNT-CM/PMS was assessed via the cycle experiments and Co ion leaching detection (Fig. S8). The leaching of Co ions was always below the detection limit of the ICP instrument (0.001 mg L^{-1}) during the six-cycle experiments. Besides, Co_1-NCNT-CM/PMS could control phenol removal at about 80% at the end of the sixth cycle. The slight decrease in the phenol degradation rate without Co ions leaching may be caused by the CNT substrate being fouled by pollutants in the later stage of the cycle experiments [24,44]. Therefore, the Co_1-NCNT-CM/PMS system possessed high efficiency, strong stability, and reusability in removing phenol.

Fig. 3b showed that the degradation effect of the Co_1-NCNT-CM/PMS process on SMX was also excellent (93.24%), but the corresponding values of CBZ (69.83%) and ATZ (41.81%) were not as expected. In the complex SE matrix (Fig. 3c), the degradation efficiency of Co_1-NCNT-CM/PMS was reduced, which may be ascribed to the unfavorable reactions between PMS/reactive species and the SE matrix. Interestingly, the removal rates of phenol (84.34%) and SMX (75.74%) in the SE matrix by Co_1-NCNT-CM/PMS were much greater than those of CBZ (35.01%) and ATZ (32.42%). We speculated that the Co_1-NCNT-CM/PMS system might be dedicated to removing phenolic and sulfonamide organic contaminants. Co_1-NCNT-CM/PMS significantly degraded five typical phenols (phenol, 2,4-DCP, BPA, BPF, and APAP) and four sulfonamides (SMX, SMZ, SDZ, and STZ) (average over 97%), much greater than CBZ and ATZ (Fig. 3d). More importantly, the initial dosages of phenolic and sulfonamide contaminants in the Co_1-NCNT-CM/PMS system were set at 10 mg L^{-1}, higher than the 5 mg L^{-1} of CBZ and ATZ. Consequently, the Co_1-NCNT-CM/PMS process manifested a superior catalytic performance on EOCs, especially for phenols and sulfonamides with high-efficiency selectivity.

3.3. *Effects of Co_1-NCNT-CM/PMS on NOM and membrane filtration*

To study the catalytic performance of the Co_1-NCNT-CM/PMS system on NOM, the removal effect of fluorescent organic matter in SE was investigated. The EEM spectra in Fig. 4a showed that CM and CM/PMS slightly reduced the intensity of SE fluorescent organics compared to raw water. Previous research has also reported that UF membranes alone cannot effectively intercept SE fluorescent organics, and PMS alone was difficult to degrade with intricate properties [10]. The Co_1-NCNT-CM/PMS possessed the best behavior in removing fluorescent organics. For quantitative analysis, three SE fluorescent components were identified by the PARAFAC method (Fig. S9a and Table S4), namely microbial-derived humic acid-like (component 1), tryptophan-like proteins (component 2), and terrestrial-derived humic-like (component 3) [45]. It was found that the CM/PMS process could reduce the fluorescence intensities of the three components by 17.90–25.22%, as described in Fig. S9b. Compared with the results of unmodified CM, the combination of NCNT- and CoCNT-modified CM with PMS enhanced the degradation rate of three fluorescence components by about 30% respectively. Co_1-NCNT-CM/PMS further promoted the degradation effect of three components, with those of 68.14%, 78.15%, and 78.16%, respectively. In summary, the Co_1-NCNT-CM/PMS system presented a significant degradation ability for the NOM.

Membrane antifouling ability was essential to examine the performance and the practical application potential of the modified CM. Direct filtration of SE by pristine CM caused a sharp decline in the normalized specific flux curve, implying severe membrane fouling in the filtration process (Fig. 4b). The CM/PMS process cannot effectively slow down the decline of membrane-specific

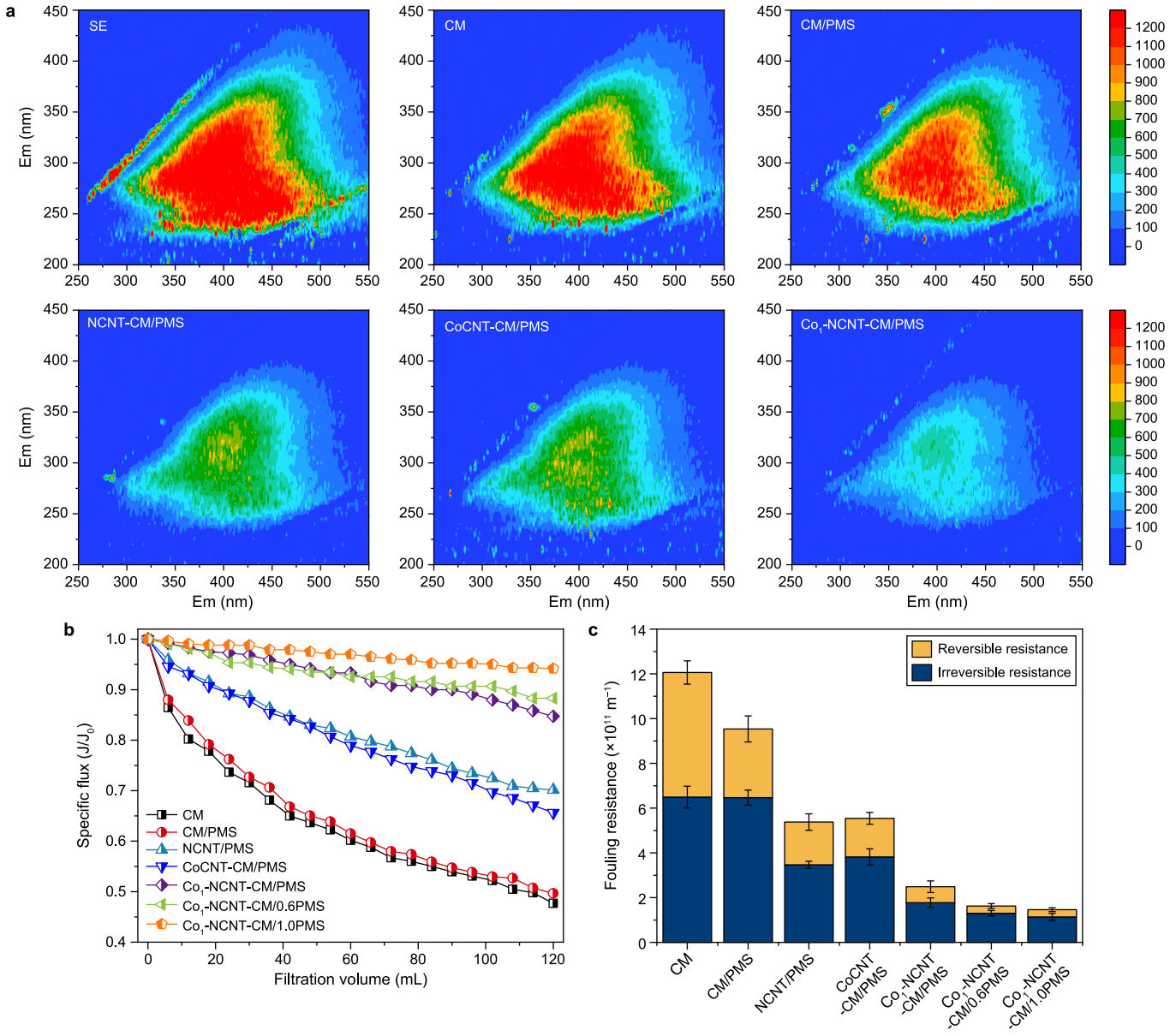

Fig. 4. **a**, SE fluorescence EEM spectra. **b**, Normalized flux decline. **c**, Membrane fouling resistance distributions. Error bars ($n = 3$).

flux. NCNT-CM/PMS and CoCNT-CM/PMS enhanced the specific flux to some extent, which remained within 65.62–70.15% of the initial flux at the end of filtration. In contrast, the Co_1-NCNT-CM/PMS system had outstanding filtration performance, and the specific flux only declined to 84.73% of the initial flux. Besides, with the increase of PMS dosage from 0.3 to 1.0 mM, the downward trends of the specific flux curves were further retarded, approaching the level. The relatively constant water flux of the Co_1-NCNT-CM/PMS process meant that the frequency of chemical cleaning and hydraulic backwashing of the membrane in actual water treatment could be reduced. Membrane fouling resistance induced by SE was quantified to analyze the state of membrane fouling under different systems (Fig. 4c). The CM/PMS process could mitigate the reversible membrane fouling, but it was ineffective for irreversible fouling. Severe irreversible membrane fouling generally requires frequent chemical cleaning to restore membrane flux, increasing operating costs [46]. NCNT- and CoCNT-modified CM/PMS mitigated the reversible and irreversible fouling resistances by 65.72–69.09% and 41.16–46.59%, respectively. Notably, Co_1-NCNT-CM/PMS showed superior performance in alleviating reversible and irreversible fouling resistances caused by SE, reducing by 87.18% and 72.67%, respectively. The increase of PMS dosage in the Co_1-NCNT-modified CM system further lightened the reversible (~94%) and irreversible membrane fouling (~80%), corresponding to the results of specific flux. This could be attributed to the boosted interaction between the high concentration of PMS and the catalyst's active sites, which was conducive to generating reactive species and improving the catalytic filtration performance [14]. Overall, the Co_1-NCNT-CM/PMS process efficiently controlled the decline of specific flux and alleviated membrane fouling from SE, proving its application potential in actual water treatment.

3.4. Contributions of the repulsive zone during the catalytic filtration process

The influence mechanisms of the Co_1-NCNT-CM/PMS system on

foulants and membrane filtration were revealed by XDLVO analysis exploring the interfacial interactions between oxidized NOM and the membrane surface. The responses of different interfacial interactions with separation distances were assessed in Fig. 5a–c. For CM filtration alone, the van der Waals (LW) interaction, acid–base (AB) interaction, and electrostatic (EL) interaction all exhibited negative values in the separation interval of 2 nm; thus, the foulants and membrane were always in the adsorption state within this proximity. This continuous adsorption state may rapidly accumulate foulants on the membrane surface to form a cake layer. The introduction of PMS caused the LW force to become positive, thus forming a mild energy barrier at a distance of around 0.06 nm from the CM surface. The existence of the energy barrier prompted the accumulated foulants to loosen on the membrane surface, reducing the possibility of forming a dense filtration cake layer. By contrast, the steep energy barrier produced in Co_1-NCNT-CM/PMS indicated that the accumulation of foulants on the membrane surface was the loosest and may create voids. This loose structure of foulants may slow the decline of specific flux and be more easily removed by hydraulic backwash, thereby mitigating the irreversible membrane fouling. Moreover, the separation distance was extended to 100 nm to investigate the contribution variations of different interfacial interactions and repulsion/attraction zones. As for the distributions of dominant interactions, it was found that the key difference between Co_1-NCNT-CM/PMS and CM was the EL interaction (Fig. S10), which might be relevant to the Co_1-NCNT-CM zeta potential (Fig. S11). The distribution of dominant forces in CM/PMS and Co_1-NCNT-CM/PMS systems was similar, with increased separation distance in LW, AB, and LW forces. The separation distance can be divided into three main regions according to the interaction force properties as the organics reached the membrane surface from the solution, which was the attractive, repulsive, and attractive zones (Fig. 5d–f). In addition, we found that the strength of various forces was negatively correlated with the separation distances, and these interactions were almost negligible when the distance exceeded 2 nm. Although a relatively wide repulsive zone (4.35–6.71 nm) appeared in the CM process, it was too far away from the membrane surface. In contrast, the entire repulsive region

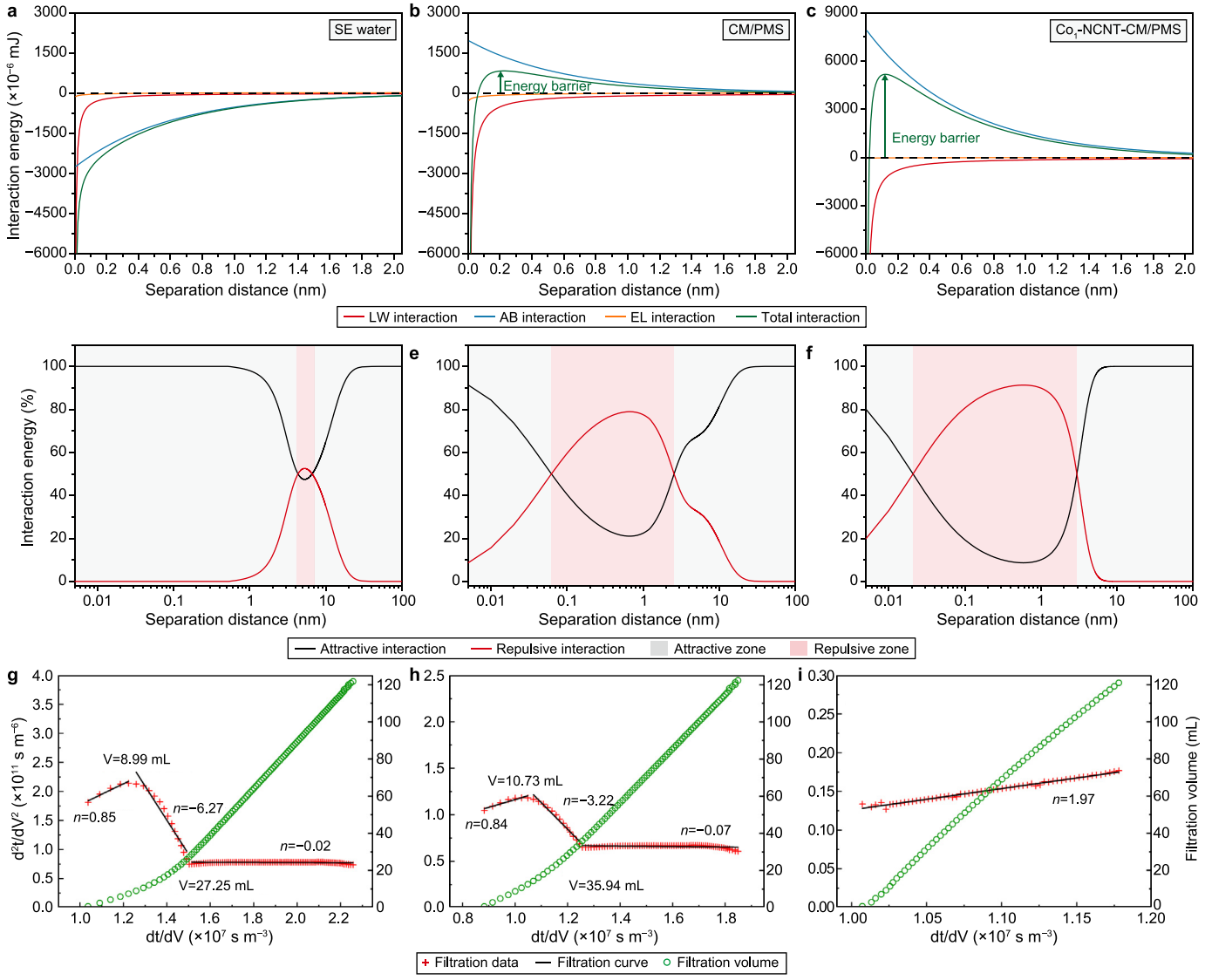

Fig. 5. **a**–**c**, Interaction energies with various separation distances: CM (**a**); CM/PMS (**b**); Co_1-NCNT-CM/PMS (**c**). **d**–**f**, The corresponding proportion of repulsive energy and attractive energy among total interaction energy: CM (**d**); CM/PMS (**e**); Co_1-NCNT-CM/PMS (**f**). **g**–**i**, Modeling fitting results of the membrane fouling patterns: CM (**g**); CM/PMS (**h**); Co_1-NCNT-CM/PMS (**i**).

(0.02−2.96 nm) under the Co_1-NCNT-CM/PMS process was wider and closer to the membrane surface. Hence, SE foulants are required to first travel through a broader repulsive zone and overcome greater repulsion forces before contacting the membrane surface during Co_1-NCNT-CM/PMS catalytic filtration. Subsequently, they passed through the narrow attraction zone (0.02 nm) and entered the centralized catalytic layer to be oxidatively degraded, relieving the pressure of the original CM size exclusion. The above findings showed that this catalytic filtration system dramatically affected the repulsive region and energy barrier between foulants and membrane, controlling the formation of the filtration cake layer and the irreversible membrane fouling.

Contributions of the repulsive zone were further verified by the fitting analysis of the pore blocking-cake layer filtration model. As described in Fig. S12, this model was able to elucidate the membrane fouling mechanism ($R^2 > 0.99$) in the catalytic filtration process. The initial membrane fouling mode due to SE was dominated by intermediate blocking ($n = 0.85$) (Fig. 5g). The fitting curve dropped sharply when the filtration reached 8.99 mL, which was the transition stage ($n < 0$) before the cake filtration mode [47]. Afterward, the fitting curve presented a smooth state ($n \approx 0$) when the filtration volume was 27.25 mL, entering a stable cake filtration mode. This proved that the previously mentioned attractions between SE organics and the membrane led to the rapid generation of the cake filtration patterns. As for the CM/PMS process, a mild energy barrier slightly delayed the occurrence of the cake filtration mode (35.94 mL in Fig. 5h). It was worth noting that the membrane fouling mode of Co_1-NCNT-CM/PMS was the complete blocking mode ($n = 1.97$). There was no transition stage and cake layer filtration mode from the beginning to the end (Fig. 5i). The main reason was that the oxidation of reactive species caused a strong energy barrier and a wide repulsive region between NOM and membrane, also corresponding to the control results of specific flux and membrane fouling resistance. Therefore, the Co_1-NCNT-CM/PMS system was promising for long-term antifouling, thereby realizing the expectation of low maintenance.

3.5. Analysis of catalytic filtration mechanism

The interaction mechanisms between PMS and catalytic membrane in the Co_1-NCNT-CM/PMS system were closely related to the role of reactive species. Besides, the coordination environment of single atoms was crucial to the selective generation of reactive species [17,48]. In this study, the reactive species generated from Co_1-NCNT-CM/PMS containing the low-coordinated Co-N_3-C sites were investigated by EPR characterization and typical quenching experiments. The EPR spectra were utilized as a direct monitor for recognizing reactive species through employing TEMP and DMPO trapping agents. Fig. 6a displayed that no obvious DMPO-$O_2^{\bullet-}$ characteristic signals were detected, indicating that the generation of $O_2^{\bullet-}$ in the catalytic system was negligible. As shown in Fig. S13a, the possible absence of $O_2^{\bullet-}$ in the Co_1-NCNT-CM/PMS system was further identified via the nitrotetrazolium blue chloride as the chemical probe [49]. The slight characteristic peaks of the DMPO-•OH and DMPO-$SO_4^{\bullet-}$ were detectable, suggesting that free radicals (•OH and $SO_4^{\bullet-}$) existed in the catalytic filtration system. By contrast, the significant triplet signal responses of the TEMP-$^1O_2$ forecasted a strong ability to generate $^1O_2$, which may be the dominant reactive species (Fig. 6b).

Quenching experiments were performed to explore the contribution of different reactive species to the degradation of EOCs (Fig. S13b). Typical scavenging agents of methanol (MeOH), tert-butanol (TBA), and L-histidine (L-His) were employed in the Co_1-NCNT-CM/PMS catalytic filtration to quench both •OH/$SO_4^{\bullet-}$, •OH, and $^1O_2$, respectively [2,50]. Interestingly, increasing the quenching dosage of MeOH and TBA from 500 mM to 2000 mM (~6666 times of PMS) still achieved ~100% removal of phenol. However, the addition of L-His strongly inhibited the phenol removal, and when the amount of L-His was increased to 30 mM (100 times of PMS), phenol was hardly degraded in the Co_1-NCNT-CM/PMS system. This proved that the oxidization of phenol was governed by $^1O_2$, which overwhelmed the contribution of free radicals, corresponding to the result of EPR (weak free radical signal). Furthermore, the removal rates of SMX, CBZ, and ATZ were all notably reduced after adding L-His, as shown in Fig. S14. The introduction of MeOH and TBA slightly inhibited the degradation of SMX but extremely affected that of CBZ and ATZ. These presented that the degradation mechanisms of different contaminants were discrepant, some of which relied on the reaction of $^1O_2$ and some were more inclined to be degraded by free radicals. As summarized in Figs. 6c, $^1O_2$ was the vital degradation reactive species for phenol and SMX, contributing 99.1% and 76.7%, respectively. The removal of CBZ and ATZ was more dependent on the effect of •OH radical, which donated 45.3% and 65.7%, respectively. As a result, the abundant $^1O_2$ and few free radicals in the Co_1-NCNT-CM/PMS system determined that it selectively and efficiently degraded phenols and sulfonamides but not CBZ and ATZ. In addition, as mentioned before, the degradation of phenol and SMX was less affected by the aqueous matrix due to the selective $^1O_2$ in the system. Nevertheless, the non-selective •OH radical was consumed more by other organic matter in actual water [51]. This was the primary reason why the degradation rate of CBZ in SE decreased from 69.83% in buffer solution to 35.01%. Therefore, the $^1O_2$-rich Co_1-NCNT-CM/PMS system largely avoided the negative influence of the actual water matrix, exhibiting good selectivity for the phenols and sulfonamides degradation under complex interference conditions.

To investigate the catalytic filtration mechanisms of Co_1-NCNT-CM/PMS deeply, DFT calculations were performed. Here, the three pyridinic-N atoms and a single Co atom were reasonably constructed to stably coordinate in the Co_1-NCNT catalyst (Fig. S15), according to the XPS and EXAFS fitting results. Fig. 6d showed that the adsorption energy (E_{ads}) of PMS on the C-C active sites of CNT itself was negative (−1.67 eV), representing that the adsorption was stable [14]. The E_{ads} values of PMS on N_3-C and Co-N_3-C sites were lower than those of PMS/C-C, which were −2.12 and −2.41 eV, respectively, attributing to the asymmetric electron distribution via the heteroatom introduction [52]. PMS was more inclined to couple with Co-N_3-C sites in Co_1-NCNT-CM to form surface-reactive complexes, which also led to the largest stretching length (1.462 Å) of O-O bond. The stretched peroxide O-O bonds in the Co_1-NCNT-CM/PMS system were readily broken to generate reactive species (•OH, $SO_4^{\bullet-}$, and $^1O_2$) [9]. Considering that selective $^1O_2$ was the dominant reactive species in the catalytic system, its possible generation pathway was deduced by the Gibbs free energies calculation. The PMS molecule spontaneously adsorbed to Co-N_3-C sites to form PMS*, which was subsequently cleaved into OH* and SO_4* moieties (Fig. 6e). The free energy profiles illustrated that these two successive steps were both thermodynamically favorable. Subsequently, the OH* moiety needed to overcome the energy barrier of 0.26 eV to convert into O*/H* and adsorb on the Co-N_3-C sites, and SO_4* was exothermically released into the water bodies in the form of H_2SO_4. After the production of intermediate O*, two possible formation pathways could happen for $^1O_2$. The first pathway involved the spontaneous adsorption of an oxygen atom at another adjacent site onto the Co_1-NCNT-O* site, which then overcame the energy barrier (0.22 eV) to produce $^1O_2$. Alternatively, the second pathway involved the initial formation of OOH* (with an energy barrier of 0.35 eV), followed by the direct desorption of H to yield $^1O_2$. The first pathway (PMS → PMS* → OH* → O* → OO* → $^1O_2$) was deemed more feasible,

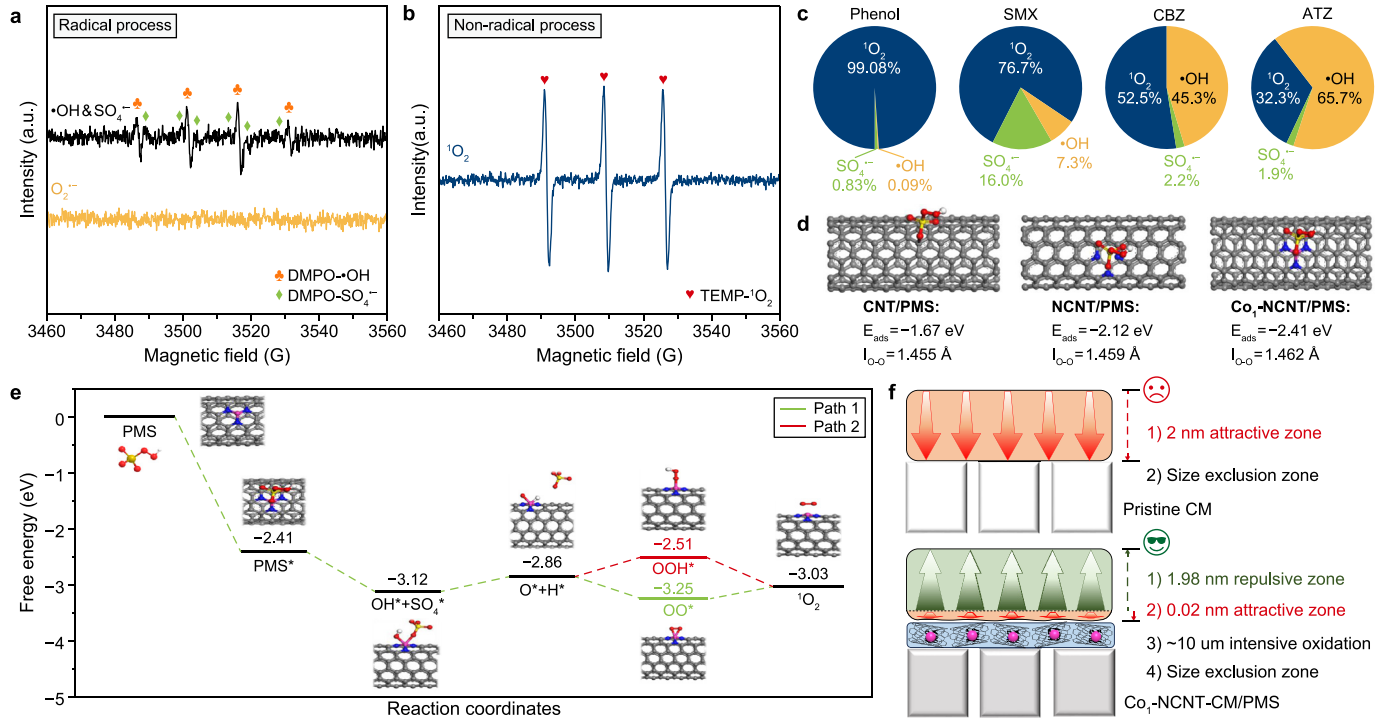

Fig. 6. **a**, EPR spectra of $O_2^{\bullet-}$, $SO_4^{\bullet-}$, and •OH. **b**, EPR spectra of $^1O_2$. **c**, Contribution of different reactive species to the degradation of contaminants. **d**, The adsorption energy of PMS on three catalysts (CNT, NCNT, and Co_1-NCNT). **e**, Possible generation mechanisms of $^1O_2$ over Co-N_3-C sites activated PMS by the Gibbs free energy calculation. **f**, Schematic diagram of multi-layer functional zones. Reaction conditions: [phenol] = [SMX] = 10 mg L^{-1}, [CBZ] = [ATZ] = 5 mg L^{-1}, [PMS] = 0.3 mmol L^{-1}, [MeOH] = [TBA] = 2 mol L^{-1}, [L-His] = 30 mmol L^{-1}, [DMPO] = [TEMP] = 10 mmol L^{-1}, pH = 7.

with the generation of the O* intermediate being a rate-determining step.

PMS tended to be adsorbed on the Co-N_3-C structure to generate a $^1O_2$-dominated reactive species system, strengthening the repulsive zone and shortening the attractive zone (Fig. 6f). The existence of the repulsion relatively alleviated the critical concentration of organic foulants in this reaction zone adjacent to the membrane surface. Besides, compared with the spontaneous accumulation of foulants in the large-scope attractive region of the pristine membrane, the narrowness of the Co_1-NCNT-CM/PMS system could minimize the accumulation of contaminants. Subsequently, the centralized oxidation layer with porous channel structure intensively enhanced the mass transfer of reactive species to degrade contaminants from the attractive zone, preventing them from directly contacting membrane pores and maintaining high permeate flux. Undegraded organic matter was finally physically separated via the membrane size exclusion. This integrated treatment mode of multi-layer functional zones (long repulsion-short attraction-intensive oxidation-size exclusion) in the Co_1-NCNT-CM/PMS system achieved layer-by-layer organic decontamination, which was essential for permeate flux and quality.

4. Conclusion

This study proposed an environmentally friendly catalytic filtration system (Co_1-NCNT-CM/PMS) without heavy metal leaching, preserving the water transmission characteristics while maintaining the high activity and stability of the tailored CM. Co_1-NCNT-CM/PMS restrained the interference of the aqueous media, enabling the efficient and selective removal of phenols and sulfonamides, thus providing the possibility for targeted removal of pollutants in intricate water matrices. Besides, Co_1-NCNT-CM/PMS significantly alleviated membrane fouling caused by SE, improving the specific flux to 84.73%. The energy barrier between foulants and membrane in the Co_1-NCNT-CM/PMS system delayed the adhesion of foulants on the catalytic membrane surface. $^1O_2$, generated through the pathway PMS → PMS* → OH* → O* → OO* → $^1O_2$, was mainly responsible for selective EOCs degradation, overlaying the contribution of free radicals. Multi-layer functional zones (long repulsion → short attraction → intensive oxidation → size exclusion) in the catalytic filtration system were identified, contributing to wastewater remediation and membrane fouling mitigation. These findings provide a novel process with on-demand selectivity for organic decontamination and offer new inspiration for single-atom catalytic membranes for future applications in actual wastewater treatments. Furthermore, this catalytic membrane system is portable and modular, making it an adaptable solution for local water treatment facilities to cope with water quality fluctuations and emergency situations.

CRediT authorship contribution statement

Jiaxuan Yang: Data Curation, Writing - Original Draft, Writing - Review & Editing. **Jing Zhao:** Data Curation, Methodology. **Hesong Wang:** Formal Analysis, Writing - Review & Editing. **Yatao Liu:** Writing - Review & Editing. **Junwen Ding:** Methodology. **Tianyi Wang:** Software. **Jinlong Wang:** Software. **Han Zhang:** Investigation. **Langming Bai:** Formal Analysis. **Heng Liang:** Conceptualization, Funding Acquisition, Resources, Supervision.

Declaration of competing interest

The authors declare that they have no known competing financial interests or personal relationships that could have appeared to influence the work reported in this paper.

Acknowledgements

This research was jointly supported by the National Natural Science Foundation of China (U22A20240; 52300001), China Postdoctoral Science Foundation (2023M730275), State Key Laboratory of Urban Water Resource and Environment (Harbin Institute of Technology) (2022TS01), and Fundamental Research Funds for the Central Universities.

Appendix A. Supplementary data

Supplementary data to this article can be found online at https://doi.org/10.1016/j.ese.2024.100416.

References

[1] K. Czuba, K. Pacyna-Iwanicka, A. Bastrzyk, M. Kabsch-Korbutowicz, A. Dawiec-Liśniewska, P. Chrobot, A. Shavandi, D. Podstawczyk, Towards the circular economy — sustainable fouling mitigation strategies in ultrafiltration of secondary effluent, Desalination 532 (2022) 115731.
[2] Y. Zhen, Z. Sun, H. Qie, Y. Zhang, C. Liu, D. Lu, W. Wang, Y. Tian, J. Ma, Selectively efficient removal of micropollutants by N-doped carbon modified catalytic ceramic membrane: synergy of membrane confinement and surface reaction, Appl. Catal., B 324 (2023) 122188.
[3] W. Song, X. Xiao, G. Wang, X. Dong, X. Zhang, Highly efficient peroxymonosulfate activation on Fe-N-C catalyst via the collaboration of low-coordinated Fe-N structure and Fe nanoparticles for enhanced organic pollutant degradation, J. Hazard Mater. 455 (2023) 131596.
[4] G. Pérez, P. Gómez, I. Ortiz, A. Urtiaga, Techno-economic assessment of a membrane-based wastewater reclamation process, Desalination 522 (2022) 115409.
[5] M. Aslam, F. Wicaksana, M. Farid, A. Wong, W.B. Krantz, Mitigation of membrane fouling by whey protein via water hammer, J. Membr. Sci. 642 (2022) 119967.
[6] A.E. Oluwalana, T. Musvuugwa, S.T. Sikwila, J.S. Sefadi, A. Whata, M.M. Nindi, N. Chaukura, The screening of emerging micropollutants in wastewater in sol plaatje municipality, northern cape, South Africa, Environ. Pollut. 314 (2022) 120275.
[7] X. Qu, P.J.J. Alvarez, Q. Li, Applications of nanotechnology in water and wastewater treatment, Water Res. 47 (12) (2013) 3931–3946.
[8] S. Aithal, Nanotechnology innovations & business opportunities : a review, Int. J. Manag. IT Eng. (IJMIE) 6 (2016) 182–204.
[9] X. Mi, P. Wang, S. Xu, L. Su, H. Zhong, H. Wang, Y. Li, S. Zhan, Almost 100% peroxymonosulfate conversion to singlet oxygen on single-atom CoN2+2 sites, Angew. Chem. Int. Ed. 60 (9) (2021) 4588–4593.
[10] J. Yang, L. Bai, J. Zhao, Y. Liu, H. Wang, G. Li, H. Liang, New insights into interfacial interaction and nanoconfinement effect in synergistic oxidation-filtration via CoFe2O4-ceramic membrane activated peroxymonosulfate, Chem. Eng. J. 461 (2023) 141846.
[11] S. Giannakis, K.-Y.A. Lin, F. Ghanbari, A review of the recent advances on the treatment of industrial wastewaters by Sulfate Radical-based Advanced Oxidation Processes (SR-AOPs), Chem. Eng. J. 406 (2021) 127083.
[12] C. Chu, J. Yang, X. Zhou, D. Huang, H. Qi, S. Weon, J. Li, M. Elimelech, A. Wang, J.-H. Kim, Cobalt single atoms on tetrapyridomacrocyclic support for efficient peroxymonosulfate activation, Environ. Sci. Technol. 55 (2) (2021) 1242–1250.
[13] C.-X. Zhao, B.-Q. Li, J.-N. Liu, Q. Zhang, Intrinsic electrocatalytic activity regulation of M–N–C single-atom catalysts for the oxygen reduction reaction, Angew. Chem. Int. Ed. 60 (9) (2021) 4448–4463.
[14] X. Peng, J. Wu, Z. Zhao, X. Wang, H. Dai, Y. Wei, G. Xu, F. Hu, Activation of peroxymonosulfate by single atom Co-N-C catalysts for high-efficient removal of chloroquine phosphate via non-radical pathways: electron-transfer mechanism, Chem. Eng. J. 429 (2022) 132245.
[15] W. Ren, G. Nie, P. Zhou, H. Zhang, X. Duan, S. Wang, The intrinsic nature of persulfate activation and N-doping in carbocatalysis, Environ. Sci. Technol. 54 (10) (2020) 6438–6447.
[16] X. Duan, H. Sun, Z. Shao, S. Wang, Nonradical reactions in environmental remediation processes: uncertainty and challenges, Appl. Catal., B 224 (2018) 973–982.
[17] Z. Wang, E. Almatrafi, H. Wang, H. Qin, W. Wang, L. Du, S. Chen, G. Zeng, P. Xu, Cobalt single atoms anchored on oxygen-doped tubular carbon nitride for efficient peroxymonosulfate activation: simultaneous coordination structure and morphology modulation, Angew. Chem. Int. Ed. 61 (29) (2022) e202202338.
[18] X. Cheng, Y. Zhang, Q. Fan, L. Wang, S. Shi, X. Luo, X. Zhu, D. Wu, H. Liang, Preparation of Co3O4@carbon nanotubes modified ceramic membrane for simultaneous catalytic oxidation and filtration of secondary effluent, Chem. Eng. J. 454 (2023) 140450.
[19] S. Zhang, M. Sun, T. Hedtke, A. Deshmukh, X. Zhou, S. Weon, M. Elimelech, J.-H. Kim, Mechanism of heterogeneous fenton reaction kinetics enhancement under nanoscale spatial confinement, Environ. Sci. Technol. 54 (17) (2020) 10868–10875.
[20] Y. Bao, W.J. Lee, T.-T. Lim, R. Wang, X. Hu, Pore-functionalized ceramic membrane with isotropically impregnated cobalt oxide for sulfamethoxazole degradation and membrane fouling elimination: synergistic effect between catalytic oxidation and membrane separation, Appl. Catal., B 254 (2019) 37–46.
[21] Y. Zhao, D. Lu, C. Xu, J. Zhong, M. Chen, S. Xu, Y. Cao, Q. Zhao, M. Yang, J. Ma, Synergistic oxidation - filtration process analysis of catalytic CuFe2O4 - tailored ceramic membrane filtration via peroxymonosulfate activation for humic acid treatment, Water Res. 171 (2020) 115387.
[22] X. Wu, K. Rigby, D. Huang, T. Hedtke, X. Wang, M.W. Chung, S. Weon, E. Stavitski, J.-H. Kim, Single-atom cobalt incorporated in a 2D graphene oxide membrane for catalytic pollutant degradation, Environ. Sci. Technol. 56 (2) (2022) 1341–1351.
[23] W. Ma, M. Sun, D. Huang, C. Chu, T. Hedtke, X. Wang, Y. Zhao, J.-H. Kim, M. Elimelech, Catalytic membrane with copper single-atom catalysts for effective hydrogen peroxide activation and pollutant destruction, Environ. Sci. Technol. 56 (12) (2022) 8733–8745.
[24] J. Yang, L. Bai, J. Zhao, Y. Liu, H. Wang, H. Zhang, G. Li, H. Liang, Cobalt oxide decorated activated carbon/peroxymonosulfate pretreatment for ultrafiltration membrane fouling control in secondary effluent treatment: insights into interfacial interaction and fouling model transformation, Sep. Purif. Technol. 316 (2023) 123820.
[25] C. Meng, B. Ding, S. Zhang, L. Cui, K.K. Ostrikov, Z. Huang, B. Yang, J.-H. Kim, Z. Zhang, Angstrom-confined catalytic water purification within Co-TiOx laminar membrane nanochannels, Nat. Commun. 13 (1) (2022) 4010.
[26] H. Wu, C. Sun, Y. Huang, X. Zheng, M. Zhao, S. Gray, Y. Dong, Treatment of oily wastewaters by highly porous whisker-constructed ceramic membranes: separation performance and fouling models, Water Res. 211 (2022) 118042.
[27] C. Sun, B. Lin, X. Zheng, Y. Dong, M. Zhao, C.Y. Tang, Robust ceramic-based graphene membrane for challenging water treatment with enhanced fouling and scaling resistance, Water Res. 243 (2023) 120348.
[28] M.B. Tanis-Kanbur, N.R. Tamilselvam, J.W. Chew, Membrane fouling mechanisms by BSA in aqueous-organic solvent mixtures, J. Ind. Eng. Chem. 108 (2022) 389–399.
[29] J.A. Brant, A.E. Childress, Assessing short-range membrane–colloid interactions using surface energetics, J. Membr. Sci. 203 (1) (2002) 257–273.
[30] C.C. Ho, A.L. Zydney, A combined pore blockage and cake filtration model for protein fouling during microfiltration, J. Colloid Interface Sci. 232 (2) (2000) 389–399.
[31] J. Hermia, Constant pressure blocking filtration law application to power-law non-Newtonian fluid, Trans. Inst. Chem. Eng. 60 (1982) 183–187.
[32] A. Zhao, J. Masa, W. Xia, A. Maljusch, M.-G. Willinger, G. Clavel, K. Xie, R. Schlögl, W. Schuhmann, M. Muhler, Spinel Mn–Co oxide in N-doped carbon nanotubes as a bifunctional electrocatalyst synthesized by oxidative cutting, J. Am. Chem. Soc. 136 (21) (2014) 7551–7554.
[33] Y. Fu, D. Xu, Y. Wang, X. Li, Z. Chen, K. Li, Z. Li, L. Zheng, X. Zuo, Single atoms anchored on cobalt-based catalysts derived from hydrogels containing phthalocyanine toward the oxygen reduction reaction, ACS Sustain. Chem. Eng. 8 (22) (2020) 8338–8347.
[34] Y. Hoe Seon, Y. Chan Kang, J.S. Cho, One-dimensional porous nanostructure composed of few-layered MoSe2 nanosheets and highly densified-entangled-N-doped CNTs as anodes for Na ion batteries, Chem. Eng. J. 425 (2021) 129051.
[35] X. Song, H. Zhang, Y. Yang, B. Zhang, M. Zuo, X. Cao, J. Sun, C. Lin, X. Li, Z. Jiang, Bifunctional nitrogen and cobalt codoped hollow carbon for electrochemical syngas production, Adv. Sci. 5 (7) (2018) 1800177.
[36] S. Chao, Z. Bai, Q. Cui, H. Yan, K. Wang, L. Yang, Hollowed-out octahedral Co/N-codoped carbon as a highly efficient non-precious metal catalyst for oxygen reduction reaction, Carbon 82 (2015) 77–86.
[37] S. Wang, Q. Jiang, S. Ju, C.-S. Hsu, H.M. Chen, D. Zhang, F. Song, Identifying the geometric catalytic active sites of crystalline cobalt oxyhydroxides for oxygen evolution reaction, Nat. Commun. 13 (1) (2022) 6650.
[38] T. Wu, S. Sun, J. Song, S. Xi, Y. Du, B. Chen, W.A. Sasangka, H. Liao, C.L. Gan, G.G. Scherer, L. Zeng, H. Wang, H. Li, A. Grimaud, Z.J. Xu, Iron-facilitated dynamic active-site generation on spinel CoAl2O4 with self-termination of surface reconstruction for water oxidation, Nat. Catal. 2 (9) (2019) 763–772.
[39] X. Liu, L. Zheng, C. Han, H. Zong, G. Yang, S. Lin, A. Kumar, A.R. Jadhav, N.Q. Tran, Y. Hwang, J. Lee, S. Vasimalla, Z. Chen, S.-G. Kim, H. Lee, Identifying the activity origin of a cobalt single-atom catalyst for hydrogen evolution using supervised learning, Adv. Funct. Mater. 31 (18) (2021) 2100547.
[40] X. Liu, Y. Deng, L. Zheng, M.R. Kesama, C. Tang, Y. Zhu, Engineering low-coordination single-atom cobalt on graphitic carbon nitride catalyst for hydrogen evolution, ACS Catal. 12 (9) (2022) 5517–5526.
[41] Y. Liu, Q. Lin, Y. Guo, J. Zhao, X. Luo, H. Zhang, G. Li, H. Liang, The nitrogen-doped multi-walled carbon nanotubes modified membrane activated peroxymonosulfate for enhanced degradation of organics and membrane fouling mitigation in natural waters treatment, Water Res. 209 (2022) 117960.
[42] Y. Zhao, D. Lu, Y. Cao, S. Luo, Q. Zhao, M. Yang, C. Xu, J. Ma, Interaction analysis between gravity-driven ceramic membrane and smaller organic matter: implications for retention and fouling mechanism in ultralow pressure-driven filtration system, Environ. Sci. Technol. 52 (23) (2018) 13718–13727.
[43] J.-C. Li, P.-X. Hou, C. Liu, Heteroatom-doped carbon nanotube and graphene-based electrocatalysts for oxygen reduction reaction, Small 13 (45) (2017)

1702002.
[44] P.R. Shukla, S. Wang, H. Sun, H.M. Ang, M. Tadé, Activated carbon supported cobalt catalysts for advanced oxidation of organic contaminants in aqueous solution, Appl. Catal., B 100 (3) (2010) 529–534.
[45] Y. Yamashita, E. Tanoue, Chemical characterization of protein-like fluorophores in DOM in relation to aromatic amino acids, Mar. Chem. 82 (3) (2003) 255–271.
[46] J. Yang, Y. Liu, J. Zhao, H. Wang, G. Li, H. Liang, Controlling ultrafiltration membrane fouling in surface water treatment via combined pretreatment of O3 and PAC: mechanism investigation on impacts of technological sequence, Sci. Total Environ. 895 (2023) 165168.
[47] S. Byun, J.S. Taurozzi, A.L. Alpatova, F. Wang, V.V. Tarabara, Performance of polymeric membranes treating ozonated surface water: effect of ozone dosage, Sep. Purif. Technol. 81 (3) (2011) 270–278.
[48] X. Dong, Z. Chen, A. Tang, D.D. Dionysiou, H. Yang, Mineral modulated single atom catalyst for effective water treatment, Adv. Funct. Mater. 32 (16) (2022) 2111565.
[49] W. Li, X. He, B. Li, B. Zhang, T. Liu, Y. Hu, J. Ma, Structural tuning of multi-shelled hollow microspheres for boosted peroxymonosulfate activation and selectivity: role of surface superoxide radical, Appl. Catal., B 305 (2022) 121019.
[50] J. Xie, Z. Liao, M. Zhang, L. Ni, J. Qi, C. Wang, X. Sun, L. Wang, S. Wang, J. Li, Sequential ultrafiltration-catalysis membrane for excellent removal of multiple pollutants in water, Environ. Sci. Technol. 55 (4) (2021) 2652–2661.
[51] J. Xie, C. Zhang, T.D. Waite, Hydroxyl radicals in anodic oxidation systems: generation, identification and quantification, Water Res. 217 (2022) 118425.
[52] K. Zhang, X. Min, T. Zhang, M. Xie, M. Si, L. Chai, Y. Shi, Selenium and nitrogen co-doped biochar as a new metal-free catalyst for adsorption of phenol and activation of peroxymonosulfate: elucidating the enhanced catalytic performance and stability, J. Hazard Mater. 413 (2021) 125294.